Few-Femtosecond XUV Pulse Pairs with Independently Tunable Topological Properties

Primož Rebernik Ribič*
Elettra-Sincrotrone Trieste, 34149 Basovizza, Trieste, Italy

Takashi Tanaka
RIKEN SPring-8 Center, Koto 1-1-1, Sayo, Hyogo 679-5148, Japan

(Received 18 January 2026; revised 16 March 2026; accepted 16 April 2026; published 11 May 2026)

By leveraging a recently developed slippage-compensation scheme in externally seeded free-electron lasers (FELs), we propose a method for generating few-femtosecond extreme-ultraviolet (XUV) pulse pairs with tunable topological properties and adjustable temporal delay. Simulations show that the topological charge l of each pulse can be independently set to $l = -1, 0, 1$, while the delay between the pulses can be tuned from a few to several tens of femtoseconds. Compared with superradiance—the only other currently viable approach for producing XUV pulse pairs with these characteristics—the proposed scheme offers greater flexibility, as it does not require driving the FEL into saturation, which typically necessitates a cascade configuration. Furthermore, when combined with pulse-to-pulse polarization switching, this approach has the potential to extend XUV studies of circular and helical dichroism in chiral systems and magnetic materials, as well as high-resolution imaging, into the few-femtosecond regime.

DOI: 10.1103/b2pw-pmxn

Over the past decade, major progress has been made in shaping extreme-ultraviolet (XUV) pulses in both the temporal and transverse domains. At these wavelengths, pulse shaping is naturally achieved using externally seeded configurations of free-electron lasers (FELs) [1,2], in which the properties of a conventional (typically UV) seed laser are transferred to the XUV FEL pulse via harmonic upconversion, most commonly high-gain harmonic generation (HGHG) [3].

This strategy has enabled, for example, the generation of strongly chirped pulses [4], phase-locked pulse pairs [5], and pulses with time-dependent polarization [6]. The resulting tailored XUV pulses have opened the way to coherent-control experiments, including the generation and manipulation of Rydberg-state wave packets [7], the probing of inner-subshell electronic coherences and their dephasing [8], and strong-field quantum control of ultrafast Rabi dynamics in helium atoms [9].

Significant advances have also been made toward controlling the transverse structure of XUV FEL radiation. Initial demonstrations included the generation of orbital-angular-momentum (OAM) radiation from spontaneous undulator emission [10], followed by OAM generation in externally seeded configurations [11–13]. Subsequent efforts have focused on producing structured light with spatially varying intensity, phase, and polarization, such as cylindrical vector beams generated using tandem undulators [14] and Poincaré beams from FELs [15]. These beam topologies have the potential to become powerful tools for studying complex magnetic structures and excitations [16–18], as well as chiral molecules [19].

Despite these advances, externally seeded FELs typically generate XUV pulses with durations of several tens of femtoseconds, limiting pulse shaping to comparable time scales. This contrasts with FELs operating in the self-amplified spontaneous emission mode at much shorter wavelengths (∼1 nm or below), where few- or subfemtosecond pulse structures [20–23] as well as ultrafast polarization [24,25] and OAM switching [26] have been demonstrated or proposed, and with high-harmonic generation (HHG) in gases [27,28], which provides few-femtosecond or attosecond pulses albeit at significantly lower flux. Although techniques such as superradiance [29,30] or chirped-pulse amplification [31] can yield shorter XUV pulses in seeded FELs, they generally offer reduced flexibility and limited wavelength tunability, making them less suitable for advanced pulse shaping. As a result, the generation of few-femtosecond XUV pulse pairs with independent control over the transverse phase structure of each pulse and tunable temporal separation remains an outstanding challenge in externally seeded FELs.

Here, we present a new method to generate few-femtosecond XUV pulse pairs with independently tunable OAM that can take the values $l = -1, 0, 1$ and adjustable

*Contact author: primoz.rebernik@elettra.eu

Published by the American Physical Society under the terms of the Creative Commons Attribution 4.0 International license. Further distribution of this work must maintain attribution to the author(s) and the published article's title, journal citation, and DOI.

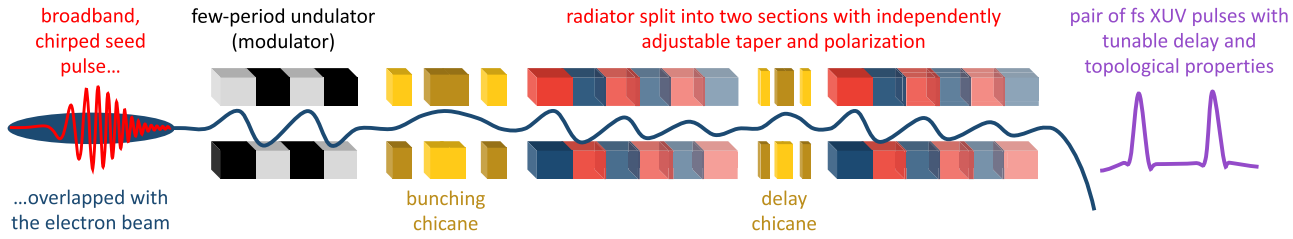


FIG. 1. Scheme to generate two delayed few-femtosecond XUV pulses with tunable OAM. The blue line shows the electron beam trajectory, with amplitude proportional to the magnetic field. Transparency of the magnets indicates the taper along the two radiators. At the end of the FEL line, the trajectory is deflected toward the beam dump.

delay from a few to several tens of femtoseconds. The scheme, shown in Fig. 1, employs a split-undulator configuration and exploits the slippage-compensation principle [32–34].

A broadband, chirped UV seed laser interacts with a relativistic electron beam in a few-period undulator (modulator) to preserve the interaction bandwidth. A chicane converts the resulting energy modulation into a chirped microbunched beam (CMB), whose density-modulation period (microbunch spacing) varies longitudinally from tail to head according to the seed-laser chirp [33]. The CMB then enters the first radiator, with a central wavelength $\lambda_{R,0}$ tuned to the nth harmonic of the seed central wavelength ($\lambda_{S,0}$), $\lambda_{R,0} = \lambda_{S,0}/n$. By appropriately tapering the radiator such that the slippage (or, equivalently, the resonant wavelength) at the radiator entrance, multiplied by n, matches the microbunch spacing in the CMB tail, and the corresponding quantity at the radiator exit matches the microbunch spacing in the CMB head, a resonant few-femtosecond pulse is generated [33]. A small chicane delays the CMB with respect to this pulse, after which it enters a second identical radiator with the same taper, generating a second pulse at a later time.

Starting from the standard expression for the resonant wavelength $\lambda_R = L/(2\gamma^2)(1 + K^2/2)$, with L the undulator period, γ the electron beam energy, and K the undulator parameter, introducing a linear taper β through $K = K_0(1 + \beta z)$, where z is the longitudinal coordinate along the undulator (and K_0 the nominal undulator parameter), and the seed-laser chirp rate α via $\omega = \omega_0 + \alpha t$, with ω_0 the instantaneous laser frequency, the following relation is obtained between the optimized taper β_{opt} and α [33],

$$\beta_{\mathrm{opt}} = \frac{1}{2\pi c^2} \frac{1 + K_0^2/2}{K_0^2} \frac{\lambda_{S,0}^2}{Ln} \alpha. \tag{1}$$

At the fundamental harmonic ($h = 1$), the radiators predominantly emit a near-Gaussian transverse mode that carries no OAM, corresponding to zero topological charge ($l = 0$). For circular polarization, higher harmonics ($h > 1$) in helical undulators are emitted off axis [10,12,13,35] and carry OAM with topological charge $l = \pm(h - 1)$, where the sign is determined by the helicity of the radiator. The resulting modes are Laguerre-Gaussian–like, exhibiting ring-shaped intensity profiles and spiraling phase structures [36].

Simulations were performed using the FEL code SIMPLEX [37–39]. We first focused on the second harmonic ($h = 2$) to demonstrate the generation of two few-femtosecond pulses with opposite topological charges ($l = \pm 1$). Similar to Ref. [33], the CMB was generated from an electron beam with an energy of 1.2 GeV, relative slice energy spread of 10^{-4}, a flat-top peak current of 800 A, normalized emittance of 0.8 mm mrad, and an average betatron function of 5 m. A seed laser with $\lambda_{S,0} = 260$ nm was stretched from its 5 fs transform-limited duration to 20 fs using a group-delay dispersion (GDD) of -35 fs^2. Seed energy and full-width half-maximum (FWHM) spot size were 0.4 mJ and 240 μm, respectively. The undulator system comprised a two-period modulator (8 cm period) followed by two identical 70-period radiators (3 cm period) with tapering matched to the seed chirp, $\beta = -7.3 \times 10^{-3}$ m^{-1} according to Eq. (1), and first chicane set to optimize the bunching.

Figure 2 shows the results for a cross-polarized configuration, in which the two radiators have opposite helicities and are tuned to $\lambda_{R,0} = 32.5$ nm (second harmonic at 16.25 nm, 76.3 eV), i.e., $n = 8$. As seen in panel (a), two pulses with peak powers of ≈5 MW and FWHM durations of ≈3 fs are generated. With the inter-radiator chicane set to zero, the ≈5 fs delay arises solely from the slippage of the first pulse over the CMB, so the pulses partially overlap. The cross-polarized configuration switches the FEL polarization from right- to left-circular between the first and second pulse, as indicated by the intensity-normalized Stokes parameter S_3, which characterizes circular polarization ($S_3 = +1$ for right circular and $S_3 = -1$ for left circular), and the topological charge l correspondingly changes sign. Panel (b) shows the combined spectral profile, while panel (c) reveals that the total time-integrated intensity has a ringlike shape, reflecting the OAM nature of each pulse.

Because the pulses carry opposite topological charges and acquire slightly different quadratic wavefront curvatures due to emission at different positions along the FEL line, the time-integrated, intensity-normalized S_1 Stokes parameter, which describes linear polarization ($S_1 = +1$

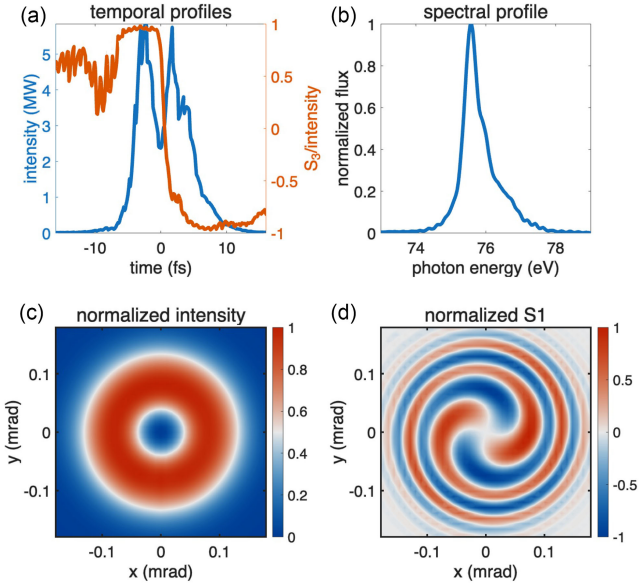


FIG. 2. (a) Temporal, (b) spectral, and (c), (d) transverse profiles of an XUV pulse pair produced by the scheme in Fig. 1 for a cross-polarized radiator configuration.

for horizontal and $S_1 = -1$ for vertical), displays a two-arm spiral pattern (panel d). Downstream of a linear polarizer, this spiral pattern appears in the intensity and serves as a direct diagnostic of the pulse structure [15], provided that the pulses overlap sufficiently to produce a measurable linear-polarization signal from their counterrotating electric fields [6].

In Fig. 2, a relatively large energy modulation was employed to enhance bunching and maximize emission at higher harmonics. This regime, however, does not permit tuning of the interpulse delay while maintaining the total output power together with balanced pulse intensities, since the strong modulation renders the bunching highly sensitive to additional dispersion from the delay chicane and the radiators. We therefore reduced the seed energy to 50 μJ and increased the spot size to 1 mm. This relaxes the demands on the seed laser and improves the stability of the transverse overlap with the electron beam. To partially compensate for the reduced energy modulation, the modulator length was increased to ten periods (still ensuring sufficient bandwidth), while the average betatron function in this region was increased to 10 m to provide more relaxed electron-beam optics. Finally, the length of each radiator was doubled to recover output power.

Figure 3 shows the temporal power profiles for the above configuration at different interpulse delays, obtained by increasing the delay chicane from 0 to 6 and then to 12 μm, corresponding to separations of ≈11, ≈19, and ≈28 fs. Because the bunching is less sensitive to additional dispersion due to the lower energy modulation, both peak intensities can be maintained at (almost) the same level for different delays without the need for additional tuning of

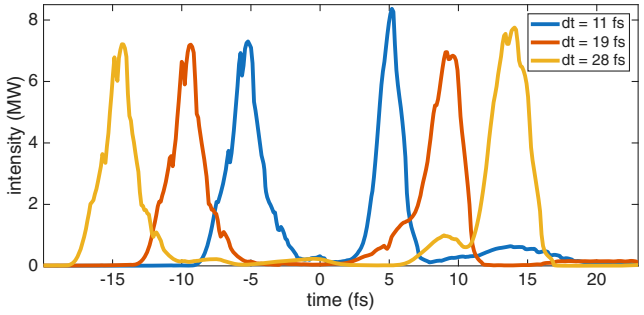


FIG. 3. Temporal profiles of XUV pulse pairs with counterrotating polarization and opposite topological charge (as in Fig. 2) for different interradiator chicane settings, demonstrating tunable pulse delay. See text for details.

FEL parameters. Together with the data shown in Fig. 2, these results demonstrate that the layout can serve as a pump-probe setup while preserving balanced output.

We note that the first chicane strength in Fig. 3 was set to keep the peak power of each pulse above 5 MW while maintaining balanced intensities for delays up to several tens of femtoseconds. Higher total power can be extracted, but at the expense of an uneven intensity distribution between the pulses (which can be advantageous when higher intensity is desired for one of the pulses). When both high power and balanced pulses are desired, fine control of the relative peak powers can be achieved by adjusting the electron-beam size in each radiator, shifting the onset of tapering (the position where $\lambda = \lambda_{R,0}$, which also slightly affects the interpulse delay), tweaking the taper strength β or using a custom-built radiator with period-by-period gap tuning [40].

Finally, in Fig. 4 we demonstrate tuning of the topological charge of individual pulses. The left column shows results for a configuration in which the first radiator is set to $\lambda_{R,0} = 16.25$ nm [and taper adjusted to $\beta = -4 \times 10^{-3}$ m^{-1}, according to Eq. (1)], corresponding to the second-harmonic wavelength used in Figs. 2 and 3, and generates a Gaussian beam with topological charge $l = 0$ at the fundamental emission wavelength ($h = 1$). The second radiator is tuned to $\lambda_{R,0} = 32.5$ nm to produce an OAM beam [41] at the second harmonic ($h = 2$) with $|l| = 1$. In this case, a single 70-period section was used for the first radiator, while the second radiator comprised two such sections. The two pulses are counterrotating, demonstrating also pulse-to-pulse polarization switching. In the second column, the second radiator (a single 70-period section) is also tuned to $\lambda_{R,0} = 16.25$ nm, resulting in two delayed counterrotating Gaussian pulses emitted at $h = 1$. Unlike in Ref. [6], the polarization switching here occurs on a few-femtosecond timescale.

Figures 2–4 demonstrate independent control of the pulses' topological charge in the range $l = -1$, 0, 1 and temporal separations up to several tens of femtoseconds.

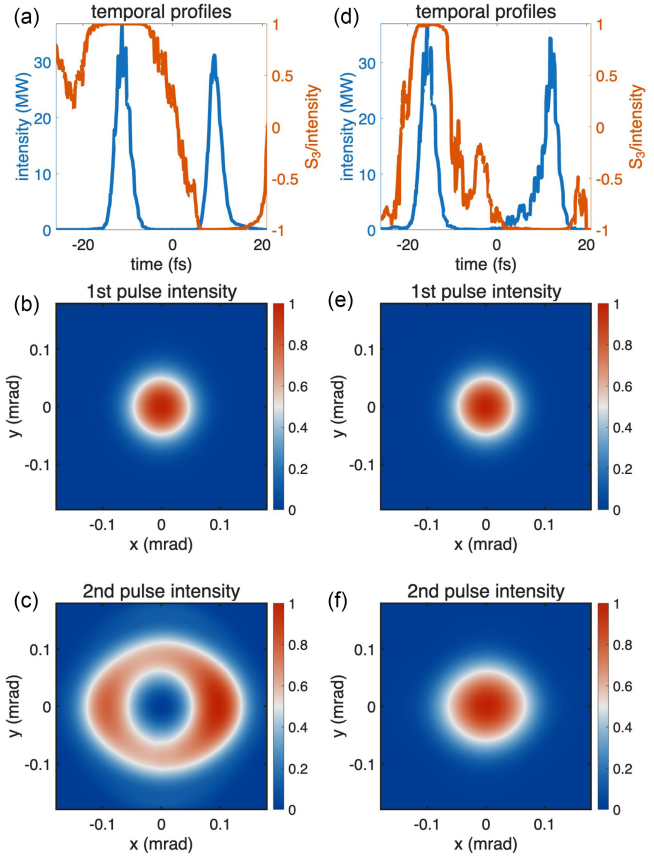


FIG. 4. Demonstration of OAM tuning. Panels (a)–(c): two delayed pulses carrying topological charges of $l = 0$ and $l = 1$. Panels (d)–(f): two delayed Gaussian pulses, both with $l = 0$. The FEL parameters (both chicane strengths and electron-beam size) were fine-tuned to obtain similar delays and peak powers for both configurations.

Higher topological charges can in principle be accessed by operating at higher harmonics of the undulator emission [45]. Alternatively, a spiral zone plate placed near the sample can increase or decrease l by the same amount for both pulses (and provide focusing at the same time [13]), further extending the tunability of the scheme. We note here that this mechanism provides a natural route to generating OAM modes in the XUV without requiring the seed (driving) laser itself to carry OAM, making the production of structured beams generally more robust than in alternative approaches based on HHG [46,47], where OAM generation requires structured and multiple driving lasers.

At this point we briefly discuss the tolerances of the scheme to various jitters: regarding the transverse overlap of the seed with the electrons and the undulator taper, the tolerances are comparable to those of standard HGHG configurations. Variations of the seed-laser phase may represent a more relevant source of fluctuations; however, we verified that varying the GDD within ~10% of the optimal value does not significantly modify the FEL pulse structure.

Other transverse profiles, such as the Hermite-Gaussian modes, can be obtained by operating the radiators in linear polarization [35]. Pulses with the same polarization can also be generated, provided they do not temporally overlap; otherwise, constructive or destructive interference may occur depending on their relative phase and will modify the overall temporal envelope. As in standard HGHG, the layout is wavelength tunable by adjusting the seed central wavelength and/or tuning the radiators to a different harmonic n and at the same time maintaining the optimized taper condition given by Eq. (1); in the latter case, the two pulses can be generated at two different wavelengths.

Structured XUV beams carrying OAM have already demonstrated sensitivity to magnetic vortices and skyrmionic textures, magnetic excitations, and helical dichroism in chiral molecules [16–19]. The ability to generate two temporally separated XUV pulses with independently tunable topological charge extends these capabilities to the time domain, opening the possibility of ultrafast measurements based on topological contrast. By comparing the response to different OAM states at controlled delays, one could track the evolution of magnetic or chiral asymmetries and extend coherent diffraction imaging to include both temporal dynamics and transverse phase sensitivity.

Concrete examples include single-shot dichroic measurements on magnetic samples or chiral molecules, using the pulse pair to simultaneously probe the response to opposite OAM states [48]. The scheme could also enable studies of more complex space-time field topologies in condensed-matter systems, for instance by introducing a controlled deviation in the electron beam trajectory after the first radiator and spatially separating the two pulses, as recently proposed in Ref. [49].

Another promising direction is the exploration of combined spin-OAM interactions. The joint interaction of spin angular momentum (SAM) and OAM gives rise to circular-helical dichroism, which can produce stronger contrast than conventional circular dichroism and may serve as a powerful probe of molecular chirality [50]. Such schemes are difficult to implement with HHG sources, where simultaneous control of OAM and circular polarization remains challenging, whereas the present approach provides a promising route toward realizing these measurements in the XUV regime.

Finally, the proposed pump-probe configuration could enable real-time measurements of molecular chirality dynamics. Recent theoretical work shows that OAM beams can monitor enantiomeric dynamics and enhance the measured asymmetry ratio compared with linearly polarized light, while the combination of OAM and SAM further strengthens the dichroic signal [51]. The generation of delayed pulses with independently controlled topological charge may therefore provide a route toward tracking

ultrafast chiral dynamics and symmetry breaking in molecular systems.

Acknowledgments—We thank Flavio Capotondi and Kevin Prince for valuable discussions on potential applications of structured XUV radiation in ultrafast studies of magnetic and chiral systems.

Data availability—The data that support the findings of this article are not publicly available. The data are available from the authors upon reasonable request.

[1] B. W. J. McNeil and N. R. Thompson, X-ray free-electron lasers, Nat. Photonics **4**, 814 (2010).
[2] N. Huang, H. Deng, B. Liu, D. Wang, and Z. Zhao, Features and futures of X-ray free-electron lasers, Innovation **2**, 100097 (2021).
[3] L. Yu *et al.*, High-gain harmonic-generation free-electron laser, Science **289**, 932 (2000).
[4] D. Gauthier, P. R. Ribič, G. De Ninno, E. Allaria, P. Cinquegrana, M. B. Danailov, A. Demidovich, E. Ferrari, L. Giannessi, B. Mahieu, and G. Penco, Spectrotemporal shaping of seeded free-electron laser pulses, Phys. Rev. Lett. **115**, 114801 (2015).
[5] D. Gauthier, P. R. Ribič, G. De Ninno, E. Allaria, P. Cinquegrana, M. B. Danailov, A. Demidovich, E. Ferrari, and L. Giannessi, Generation of phase-locked pulses from a seeded free-electron laser, Phys. Rev. Lett. **116**, 024801 (2016).
[6] G. Perosa *et al.*, Femtosecond polarization shaping of free-electron laser pulses, Phys. Rev. Lett. **131**, 045001 (2023).
[7] M. Dumergue *et al.*, Wave-packet manipulation of He Rydberg states by a seeded free-electron laser, Phys. Rev. Res. **6**, 043323 (2024).
[8] A. Wituschek *et al.*, Tracking attosecond electronic coherences using phase-manipulated extreme ultraviolet pulses, Nat. Commun. **11**, 883 (2020).
[9] F. Richter *et al.*, Strong-field quantum control in the extreme ultraviolet domain using pulse shaping, Nature (London) **636**, 337 (2024).
[10] J. Bahrdt, K. Holldack, P. Kuske, R. Müller, M. Scheer, and P. Schmid, First observation of photons carrying orbital angular momentum in undulator radiation, Phys. Rev. Lett. **111**, 034801 (2013).
[11] E. Hemsing, A. Knyazik, M. Dunning, D. Xiang, A. Marinelli, C. Hast, and J. Rosenzweig, Coherent optical vortices from relativistic electron beams, Nat. Phys. **9**, 549 (2013).
[12] E. Hemsing, M. Dunning, C. Hast, T. Raubenheimer, and D. Xiang, First characterization of coherent optical vortices from harmonic undulator radiation, Phys. Rev. Lett. **113**, 134803 (2014).
[13] P. Rebernik Ribič, B. Rösner, D. Gauthier, E. Allaria, F. Döring, L. Foglia, L. Giannessi, N. Mahne, M. Manfredda, C. Masciovecchio, R. Mincigrucci, N. Mirian, E. Principi, E. Roussel, A. Simoncig, S. Spampinati, C. David, and G. De Ninno, Extreme-ultraviolet vortices from a free-electron laser, Phys. Rev. X **7**, 031036 (2017).
[14] S. Matsuba, K. Kawase, A. Miyamoto, S. Sasaki, M. Fujimoto, T. Konomi, N. Yamamoto, M. Hosaka, and M. Katoh, Generation of vector beam with tandem helical undulators, Appl. Phys. Lett. **113**, 021106 (2018).
[15] J. Morgan, P. Rebernik Ribič, F. Capotondi, A. Brynes, M. Manfredda, G. De Ninno, L. Novinec, M. Pancaldi, E. Pedersoli, A. Simoncig, C. Spezzani, M. Zangrando, and E. Hemsing, Poincaré beams from a free electron laser, Nat. Photonics **19**, 946 (2025).
[16] M. Fanciulli *et al.*, Observation of magnetic helicoidal dichroism with extreme ultraviolet light vortices, Phys. Rev. Lett. **128**, 077401 (2022).
[17] M. Fanciulli *et al.*, Magnetic vortex dynamics probed by time-resolved magnetic helicoidal dichroism, Phys. Rev. Lett. **134**, 156701 (2025).
[18] A. A. Sirenko, P. Marsik, C. Bernhard, T. N. Stanislavchuk, V. Kiryukhin, and S.-W. Cheong, Terahertz vortex beam as a spectroscopic probe of magnetic excitations, Phys. Rev. Lett. **122**, 237401 (2019).
[19] J. Rouxel, B. Rösner, D. Karpov, C. Bacellar, G. Mancini, F. Zinna, D. Kinschel, O. Cannelli, M. Oppermann, C. Svetina, A. Diaz, J. Lacour, C. David, and M. Chergui, Hard X-ray helical dichroism of disordered molecular media, Nat. Photonics **16**, 570 (2022).
[20] S. Huang, Y. Ding, Y. Feng, E. Hemsing, Z. Huang, J. Krzywinski, A. A. Lutman, A. Marinelli, T. J. Maxwell, and D. Zhu, Generating single-spike hard X-ray pulses with nonlinear bunch compression in free-electron lasers, Phys. Rev. Lett. **119**, 154801 (2017).
[21] J. Duris *et al.*, Tunable isolated attosecond X-ray pulses with gigawatt peak power from a free-electron laser, Nat. Photonics **14**, 30 (2020).
[22] A. Malyzhenkov, Y. P. Arbelo, P. Craievich, P. Dijkstal, E. Ferrari, S. Reiche, T. Schietinger, P. Juranić, and E. Prat, Single- and two-color attosecond hard X-ray free-electron laser pulses with nonlinear compression, Phys. Rev. Res. **2**, 042018(R) (2020).
[23] J. Yan, W. Qin, Y. Chen, W. Decking, P. Dijkstal, M. Guetg, I. Inoue, N. Kujala, S. Liu, T. Long, N. Mirian, and G. Geloni, Terawatt-attosecond hard X-ray free-electron laser at high repetition rate, Nat. Photonics **18**, 1293 (2024).
[24] N. Sudar, R. Coffee, and E. Hemsing, Coherent X rays with tunable time-dependent polarization, Phys. Rev. Accel. Beams **23**, 120701 (2020).
[25] J. Morgan and B. W. J. McNeil, Attosecond polarization modulation of x-ray radiation in a free-electron laser, Phys. Rev. Accel. Beams **24**, 010701 (2021).
[26] J. Morgan and B. W. J. McNeil, X-ray pulse generation with ultra-fast flipping of its orbital angular momentum, Opt. Express **30**, 31171 (2022).
[27] M. Ferray, A. L'Huillier, X. F. Li, L. A. Lompre, G. Mainfray, and C. Manus, Multiple-harmonic conversion of 1064 nm radiation in rare gases, J. Phys. B **21**, L31 (1988).
[28] J. Li, J. Lu, A. Chew, S. Han, J. Li, Y. Wu, H. Wang, S. Ghimire, and Z. Chang, Attosecond science based on high harmonic generation from gases and solids, Nat. Commun. **11**, 2748 (2020).
[29] R. Bonifacio, B. W. J. McNeil, and P. Pierini, Superradiance in the high-gain free-electron laser, Phys. Rev. A **40**, 4467 (1989).

[30] N. S. Mirian *et al.*, Generation and measurement of intense few-femtosecond superradiant extreme-ultraviolet free-electron laser pulses, Nat. Photonics **15**, 523 (2021).
[31] D. Gauthier *et al.*, Chirped pulse amplification in an extreme-ultraviolet free-electron laser, Nat. Commun. **7**, 13688 (2016).
[32] T. Tanaka, Proposal to generate an isolated monocycle x-ray pulse by counteracting the slippage effect in free-electron lasers, Phys. Rev. Lett. **114**, 044801 (2015).
[33] T. Tanaka and P. R. Ribič, Shortening the pulse duration in seeded free-electron lasers by chirped microbunching, Opt. Express **27**, 30875 (2019).
[34] P. R. Ribič and T. Tanaka, Isolated single-cycle extreme-ultraviolet pulses from undulator radiation, Opt. Lett. **45**, 5234 (2020).
[35] S. Sasaki and I. McNulty, Proposal for generating brilliant X-ray beams carrying orbital angular momentum, Phys. Rev. Lett. **100**, 124801 (2008).
[36] L. Allen, M. W. Beijersbergen, R. J. C. Spreeuw, and J. P. Woerdman, Orbital angular momentum of light and the transformation of Laguerre-Gaussian laser modes, Phys. Rev. A **45**, 8185 (1992).
[37] T. Tanaka, SIMPLEX: Simulator and postprocessor for free-electron laser experiments, J. Synchrotron Radiat. **22**, 1319 (2015).
[38] T. Tanaka, Numerical methods for free electron laser simulations, J. Electromagn. Waves Appl. **32**, 371 (2018).
[39] T. Tanaka, Accelerating the convergence of free electron laser simulations by retrieving a spatially coherent component of microbunching, Phys. Rev. Accel. Beams **27**, 030703 (2024).
[40] T. Tanaka, Y. Kida, R. Kinjo, T. Togashi, H. Tomizawa, S. Hashimoto, S. Miyamoto, S. Okabe, and Y. Tanaka, Development of an undulator with a variable magnetic field profile, J. Synchrotron Radiat. **28**, 404 (2021).
[41] The slight asymmetry of the OAM mode observed in Fig. 4(c) indicates a small admixture of additional modes (at the few-percent energy level), consistent with previous studies of OAM generation in undulators (see, e.g., Refs. [13,42–44]).
[42] E. Hemsing, A. Marinelli, and J. B. Rosenzweig, Generating optical orbital angular momentum in a high-gain free-electron laser at the first harmonic, Phys. Rev. Lett. **106**, 164803 (2011).
[43] P. R. Ribič, D. Gauthier, and G. De Ninno, Generation of coherent extreme-ultraviolet radiation carrying orbital angular momentum, Phys. Rev. Lett. **112**, 203602 (2014).
[44] C. Xu, J. Yan, G. Geloni, C. Lechner, and H. Deng, Spatiotemporal shaping of attosecond X-rays with time-dependent orbital angular momentum, arXiv:2508.19020v2.
[45] Undesired harmonics, such as the fundamental in case of Fig. 2, are typically removed using standard spectral filters before reaching the experimental station, as done in Refs. [13,15]. A variety of filters is available at FEL facilities, and for many experiments, partial filtering is sufficient, particularly when the measurements are energy resolved.
[46] F. Kong, C. Zhang, F. Bouchard, Z. Li, G. G. Brown, D. H. Ko, T. J. Hammond, L. Arissian, R. W. Boyd, E. Karimi, and P. B. Corkum, Controlling the orbital angular momentum of high harmonic vortices, Nat. Commun. **8**, 14970 (2017).
[47] D. Gauthier, P. R. Ribič, G. Adhikary, A. Camper, C. Chappuis, R. Cucini, L. F. DiMauro, G. Dovillaire, F. Frassetto, R. Géneaux, P. Miotti, L. Poletto, B. Ressel, C. Spezzani, M. Stupar, T. Ruchon, and G. De Ninno, Tunable orbital angular momentum in high-harmonic generation, Nat. Commun. **8**, 14971 (2017).
[48] P. V. Demekhin, A. N. Artemyev, A. Kastner, and T. Baumert, Photoelectron circular dichroism with two overlapping laser pulses of carrier frequencies ω and 2ω linearly polarized in two mutually orthogonal directions, Phys. Rev. Lett. **121**, 253201 (2018).
[49] L. Foglia *et al.*, Nanoscale polarization transient gratings, Nat. Commun. **15**, 10742 (2024).
[50] L. Ye, J. R. Rouxel, S. Asban, B. Rösner, and S. Mukamel, Probing molecular chirality by orbital-angular-momentum-carrying X-ray pulses, J. Chem. Theory Comput. **15**, 4180 (2019).
[51] X. Jiang, Y. Nam, J. R. Rouxel, H. Yong, and S. Mukamel, Time-resolved enantiomer-exchange probed by using the orbital angular momentum of X-ray light, Chem. Sci. **14**, 11067 (2023).